Available online at www.sciencedirect.com
ScienceDirect
Trans. Nonferrous Met. Soc. China 33(2023) 3570−3582
Transactions of Nonferrous Metals Society of China
www.tnmsc.cn

Preparation of sillenite-type $Bi_{12}MnO_{20}$ with enhanced photocatalytic activity for removal of organic pollutants via superoxide radicals

Jing ZHAN[1], Huan-wei WANG[1], Qi-hou LI[1], Zhi-jian WANG[2], Xin FANG[1]

1. School of Metallurgy and Environment, Central South University, Changsha 410083, China;
2. Hunan Rare Earth Metal Material Research Institute, Changsha 410083, China

Received 3 November 2022; accepted 26 July 2023

Abstract: Sillenite-type photocatalytic material $Bi_{12}MnO_{20}$ with photo-absorptive ability in the spectrum range of 200−2200 nm was prepared by wet ball milling followed by calcination. The crystal structure of $Bi_{12}MnO_{20}$ can be viewed as the metastable cubic γ-Bi_2O_3 with the incorporation of Mn^{4+} into tetrahedral sites. The entry of Mn^{4+} into γ-Bi_2O_3 crystal creates a sub-bandgap of 1.25 eV appearing in the energy band structure of $Bi_{12}MnO_{20}$. The $Bi_{12}MnO_{20}$ photocatalyst can accelerate the transformation of O_2 in solution into superoxide radicals ($\cdot O_2^-$), thereby improving charge separation and transfer during photocatalytic degradation. As a result, the degradation rate of over 95% to the malachite green (MG) with a concentration of 10 mg/L in the pH=8 solution by $Bi_{12}MnO_{20}$ is achieved under simulated sunlight. After four cycles of photo-degradation, the removal rate of MG by $Bi_{12}MnO_{20}$ remains at 74.9%.
Key words: $Bi_{12}MnO_{20}$; photocatalysis; degradation; energy band; superoxide radical

1 Introduction

Organic wastewater from the leather making, printing and dyeing industry becomes a prominent part of environmental pollution due to its non-hydrolyzable and difficult-to-removal problems [1]. Several methods, such as physical adsorption [2], chemical removal [3] and electrochemical oxidation [4] have been applied to eliminating organic pollution. However, negative effects followed by these methods are the formation of toxic secondary pollutants and excessive treatment cost [5]. Since the first use of TiO_2 as photocatalysts to degrade polychlorinated biphenyls under UV radiation, photocatalysis has emerged as a green alternative for the degradation of hazardous water-soluble dyes and other toxic organic compounds. The solar energy absorbed on the surface of the photocatalyst results in the excitation of electrons from the valence band to the conduction band leaving behind the holes. These generated holes with high redox potential are responsible for the oxidation of organic molecules into harmless and low relative molecular mass products. Up to now, UV-photocatalytic systems have been studied extensively, and several photocatalysts with outstanding photocatalytic properties have been found, such as TiO_2 [6] and ZnO [7]. However, TiO_2 and ZnO have disappointing photocatalytic activity in visible (Vis) light and near-infrared (NIR) light accounting for approximately 90% of the full solar spectrum due to their wide bandgaps (E_{TiO_2}>3.2 eV, E_{ZnO}>3.37 eV) [8,9]. Hence, it is of great practical significance to develop photocatalysts with full spectrum response.

Semiconductors with narrow bandgap are extremely interesting candidates for the design of full-spectrum responsive photocatalysts, but the problem of fast recombination between photo-

Corresponding author: Qi-hou LI, Tel: +86-18975185836, E-mail: liqihou@csu.edu.cn
DOI: 10.1016/S1003-6326(23)66355-1

induced holes and electrons follows. Superoxide anion radical($\cdot O_2^-$) is a kind of important reactive oxygen ion formed by photo-induced electrons reducing oxygen molecules in solution. The formation of $\cdot O_2^-$ can not only suppress the recombination between hole and electron but also increase the number of oxidized species for attacking organic molecules, which can enhance the photocatalytic degradation efficiency. CUI et al [10] achieved the complete degradation of Rhodamine B (RhB) under visible light owing to producing $\cdot O_2^-$ as new oxidized species by the sufficient potential for photogenerated electrons in BiOCl/BiOBr heterojunction. However, due to its difficulty in preparation and poor chemical stability, its further application is hindered.

Many modification attempts aimed at promoting the production of $\cdot O_2^-$, such as semiconductor coupling and coating, have been used to improve the photocatalytic activity of narrow bandgap semiconductors, but the further application of the candidates is limited due to their difficulty in the preparation and poor chemical stability [11]. Among the developed photocatalysts, bismuth-based materials have become potential photocatalysts with visible and even near-infrared light response due to their inert electron effect of the two lone electrons occupied in the 6s orbital, such as BiOX (X=Cl, Br and I), Bi_2S_3, Bi_2O_3, $BiWO_3$, and $Bi_{12}MO_{20}$ (M=Mn, Ti, Mo, Zn, Fe, etc.) [12]. Recently, sillenite-type photocatalytic materials $Bi_{12}MO_{20}$ are considered as the most promising photocatalysts with their unique crystal structure and remarkable visible-light absorption ability, such as $Bi_{12}TiO_{20}$, $Bi_{12}CoO_{20}$ and $Bi_{12}FeO_{20}$ [13−15]. A continuous valence band in $Bi_{12}MO_{20}$ formed by Bi 6s hybridizing with O 2p at the top of the valence band displays a higher valence band and narrower bandgap than that formed by the O 2p orbital [16,17]. At the same time, the carrier separation efficiency of sillenite photocatalysts can be improved by M-element species changing their physicochemical properties such as electronic structure, energy band structure, and electronegativity of $Bi_{12}MO_{20}$ materials [18]. As a transition metal element, Mn can generate photoelectrons in Vis-NIR light by its energy level jump with a variety of oxidation states, which can not only extend the absorption sidebands to the visible range but also adjust the potential of photo-induced electrons to form $\cdot O_2^-$ [16]. WU et al [17] reported that $Bi_{12}MnO_{20}$ can effectively decompose ARG and Cr(VI) under irradiation. However, the mechanism of its enhancing photocatalytic activity still needs further exploration. Given the advantages mentioned above, $Bi_{12}MnO_{20}$ photocatalyst with full spectral response will be prepared by wet ball milling followed by the thermal decomposition method in this work. At the same time, the photocatalytic activity and the mechanism for enhancing the degradation efficiency of organic pollutants on $Bi_{12}MnO_{20}$ photocatalyst will be investigated using malachite green (MG) dyes as the model pollutant. In particular, the contribution of Mn ions for promoting the generation of superoxide radicals and broadening optical absorption will be addressed by the photoelectric properties of $Bi_{12}MnO_{20}$ and γ-Bi_2O_3. This study will offer a new way to design efficient photocatalysts with full spectrum response.

2 Experimental

2.1 Chemicals

The bismuth oxalate precursor was self-made in the laboratory, and the relevant details have been published in previous work [19]. Manganese carbonate ($MnCO_3$), bismuth oxide (Bi_2O_3), manganese dioxide (MnO_2), malachite green (MG), RhB, tetracycline hydrochloride (TC-HCl), p-benzoquinone (BQ), ammonium oxalate (AO), isopropyl alcohol (IPA) and absolute ethanol were analytical grade. The ultrapure water used in the experiment was from the public water purification system.

2.2 Materials synthesis

The sillenite-type $Bi_{12}MnO_{20}$ photocatalysts were prepared by a facile and scalable wet ball milling followed by a calcination method [19,20]. The preparation process of the $Bi_{12}MnO_{20}$ sample is shown in Fig. 1. Typically, 19.41 mg bismuth oxalate precursor, 0.23 mg manganese carbonate, and 20 mL ethanol were put into a 250 mL ball mill tank. Then, the tank was placed in the ball milling equipment and operated at 400 r/min for 24 h. The precursor of $Bi_{12}MnO_{20}$ was obtained by drying the mixture with a tank at 80 °C for 10 h after ball milling. Finally, the resultant precursor was calcined in the air atmosphere at different temperatures (400,

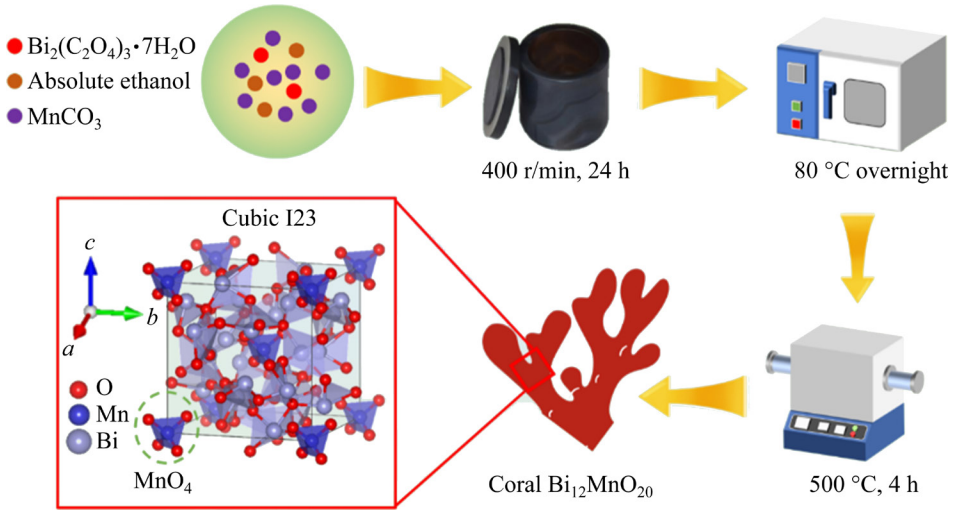

Fig. 1 Preparation route of sillenite-type $Bi_{12}MnO_{20}$

500, 600, 650, 700 °C) for 2 h to obtain a series of samples that are named as follows: BMO-400, BMO-500, BMO-600, BMO-650, and BMO-700.

2.3 Materials characterization

The TG-DSC curve was measured by a synchronous thermal analyzer (WATERS SDT 650) with the parameters varying from room temperature to 800 °C and a heat rate of 5 °C/min. The crystalline structure of materials was determined using a Rigaku-TTR III powder X-ray diffractometer (XRD) with Cu K_α radiation (λ=1.54184 Å, 40 kV, 250 mA), and scanned over a range of 10°−80° at a scan rate of 10 (°)/min. The morphology, elemental distribution, and microstructure of composites were surveyed on a high-resolution field emission scanning electron microscope (FESEM JEOL JSM−7900F) equipped with the EDS energy dispersive X-ray spectrometer and transmission electron microscopy (TEM; JEM−100CX II). The concentration of dissolved organic carbon was measured by a total organic carbon (TOC) analyzer (TOC-L, Shimadzu). The X-ray photoelectron spectrometer (XPS, Thermo ESCALAB 250XI) was used to determine the valence state of the relative element and valence band information of the sample. Photoluminescence (PL) spectra were obtained by the steady/state transient fluorescence spectrometer (FLSP920, Edinburgh Instruments) under the excitation of a hydrogen flash lamp with a wavelength of 406.2 nm. The UV-Vis-Nir diffuse reflection spectra (DRS) were obtained by a UV-Vis spectrophotometer (Shimadzu UV3600) with a wavelength range of 200−2500 nm. The specific surface area and pore size of the sample were collected by an automatic specific surface area and pore size analyzer (QUADRASORB Evo), respectively. Electron spin resonance (ESR) spectra were conducted by an electron paramagnetic resonance spectrometer (Bruker A300) to determine the types of active groups in the degradation process. A laser particle size analyzer (Mastersizer2000) was used to analyze the particle size distribution of different specimens. The Fourier infrared spectroscopy was investigated using an instrument (Nicolet IS 10) with a range of 500−3000 nm. The Mott-Schottky (MS) curve, electrochemical impedance spectroscopy (EIS) and transient photocurrent were brought by an electrochemical workstation (CHI660C).

2.4 Photocatalytic experiment

All photocatalytic degradation experiments of the as-prepared samples were carried out in a photochemical reactor using a 500W xenon lamp as the sunlight-simulated radiation source. Firstly, 0.2 g of the photocatalyst was dispersed in 100 mL simulated wastewater with 10 mg/L dyes. Then, the suspension was stirred vigorously in a dark environment for 30 min to achieve the adsorption−desorption balance between the catalyst and solution. Next, the xenon lamp was turned on to start the photocatalytic reaction. 10 mL of the suspension was taken out after 60 min and centrifuged at 8000 r/min for 6 min. 3 mL of supernatant after centrifugation was placed in a

cuvette and the absorbance was measured with UV-Vis absorbance spectroscopy at the maximum absorption wavelength of the organic substrate directly. The effects of solution pH, $Bi_{12}MnO_{20}$ concentration, simulated wastewater concentration, and dye type on the degradation efficiency were investigated.

The stability and reusability of the as-prepared sample were investigated by recycling experiments. The details of the experiment referred to a typical photocatalysis test. The sample after the degradation experiment was collected by centrifugal separation 3 times (8000 r/min, 10 min) and drying (60 °C, 12 h). The collected sample was used in the four repeated degradation experiments for evaluating the reusability of $Bi_{12}MnO_{20}$.

The radical species trapping experiments were conducted to estimate the active species in the photocatalytic degradation process. Superoxide radicals ($\cdot O_2^-$), holes (h^+), and hydroxyl ($\cdot OH$) in the solution can be captured by p-benzoquinone (BQ), ammonium oxalate (AO), and isopropanol (IPA), respectively. In a typical experiment, 0.2 g of the as-synthesized photocatalysts were added to 100 mL of organic solution, then 10 mL of 1 mol/L scavenger solution was added to the suspension.

3 Results and discussion

3.1 Morphology and structure

Figure 2 shows the structure and morphology of the samples. As shown in Fig. 2(a), $Bi_{12}MnO_{20}$ belongs to the rich-bismuth compound based on γ-Bi_2O_3 structure with Mn element located in the center of tetrahedral interstices. For the crystal structure of $Bi_{12}MnO_{20}$, the entry of Mn^{4+} (Mn: 0.46 A,) leads to perturbation of the Bi — O polyhedral network connected to the MnO_4 tetrahedron in the lattice [19]. In addition, the radius of Mn ions is generally smaller than that of other transition metal ions (Ti: 0.605 Å, Mo: 0.65 Å, Zn: 0.74 Å, Fe: 0.645 Å, Bi: 1.03 A), the deformation of Bi—O polyhedron network is more likely to occur in $Bi_{12}MnO_{20}$ than that in other sillenites [13−18]. Moreover, the position of the conduction and valence band will shift up or down respectively due to the change of the lone electron pairs state caused by the perturbation of the Bi—O polyhedron network [20]. As shown in Fig. S1 of supplementary information (SI), a continuous mass loss was observed as the temperature increased. The endothermic peaks at 146.1 °C (mass loss: 2%) and 261.46 °C (mass loss: 26.1%) can be assigned to the removal of water of crystallization and the release of CO_2 and H_2O, respectively. When the temperature exceeded 300 °C, $Bi_{12}MnO_{20}$ was obtained by the interaction of bismuth and manganese oxide. As displayed in Fig. 2(b), the thermolysis product at 400 °C displays a mixture of Bi_2O_3 and $Bi_{12}MnO_{20}$. The main diffraction peaks for the products obtained above 500 °C located at 24.65°, 27.62°, 30.31°, 32.81° and 52.22° correspond to the (220), (310), (222), (321) and (035) planes of $Bi_{12}MnO_{20}$ (JCPDS No.82-1024), respectively, and no other impurity peak appears, indicating that pure $Bi_{12}MnO_{20}$ is formed.

Figures 2(c−g) and Fig. S2 of SI display that the size of coral-like BMO increases with the temperature from 400 to 700 °C. The element mapping images (Fig. 2(h)) reveal that Bi, Mn and O are uniformly dispersed in the coral structure, which is further confirmed by the TEM image (Fig. 2(i)). The lattice spacing of 0.273 and 0.294 nm shown in the HRTEM images (Figs. 2(j) and (k)) corresponds to the (321) and (322) crystal planes of $Bi_{12}MnO_{20}$, respectively, indicating the formation of $Bi_{12}MnO_{20}$. N_2 adsorption−desorption curves (Fig. S3 of SI) indicate that BMO-500 has the largest specific surface area (3.585 m^2/g) and pore volume (0.02 cm^3/g), which can not only provide more transport channels to increase the mass transfer rate of reactants and products but also increase active sites to accelerate the photocatalytic degradation [21].

The surface chemical valance state of $Bi_{12}MnO_{20}$ was analyzed by XPS as shown in Fig. 3. As shown in Fig. 3(a), the signature peaks for Bi 4f (~160 eV), Mn 2p (~681 eV) and O 1s (~530 eV) show the coexistent of Bi, Mn and O in the catalyst without impurity elements. The characteristic peaks of the binding energy at 158.6 and 163.9 eV in Fig. 3(b) correspond to the Bi $4f_{7/2}$ and Bi $4f_{5/2}$ orbitals of Bi^{3+} in $Bi_{12}MnO_{20}$, respectively [22,23]. The O 1s peak at 530.3 eV can be assigned to the Bi — O — Bi bond bridges oxygen, and the characteristic peak at 529.3 eV can be attributed to the binding energy of oxygen in the Mn—O—Bi framework (Fig. 3(b)). The entry of Mn^{4+} into the bismuth oxide lattice can change the binding energy between oxygen and metal, leading to the electron

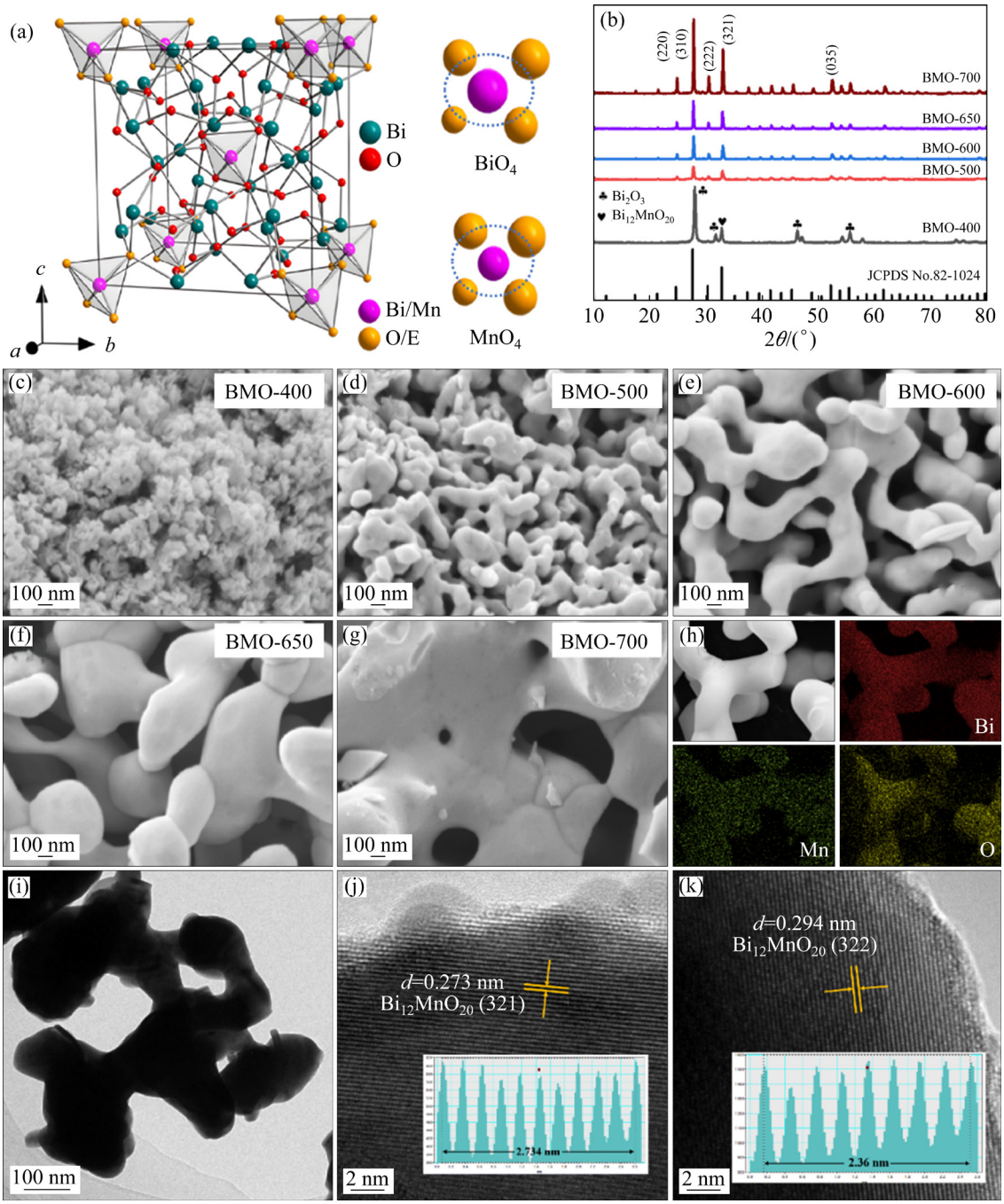

Fig. 2 Structural analysis and morphological characterization of samples: (a) Crystal structure of $Bi_{12}MnO_{20}$; (b) XRD patterns of BMO-T samples; (c−g) SEM images of BMO-T, respectively; (h−k) Mapping images, TEM and HRTEM images of BMO-500, respectively

reduction potential on CB shifting to a more negative position [22]. Moreover, the Mn $2p_{1/2}$ and Mn $2p_{2/3}$ characteristic peaks at 653.6 and 642.0 eV correspond to the Mn^{4+} state in the $Bi_{12}MnO_{20}$ phase (Fig. 3(d)). The 3d orbit of Mn^{4+} in tetrahedron is inclined to splitting into e_g and t_{2g} orbit. An intermediate band (IB) is formed due to the entry of e_g orbit occupied by the electrons into the bandgap when the t_{2g} with higher energy hybridizes with CB, improving photocatalytic activity with the lower-energy light [23,24].

3.2 Photo-response

Figure 4 shows tauc plots for the bandgap, UV-vis-Nir and PL spectra of $Bi_{12}MnO_{20}$. As can be seen from Fig. 4(a), two bandgap values of 2.0 and

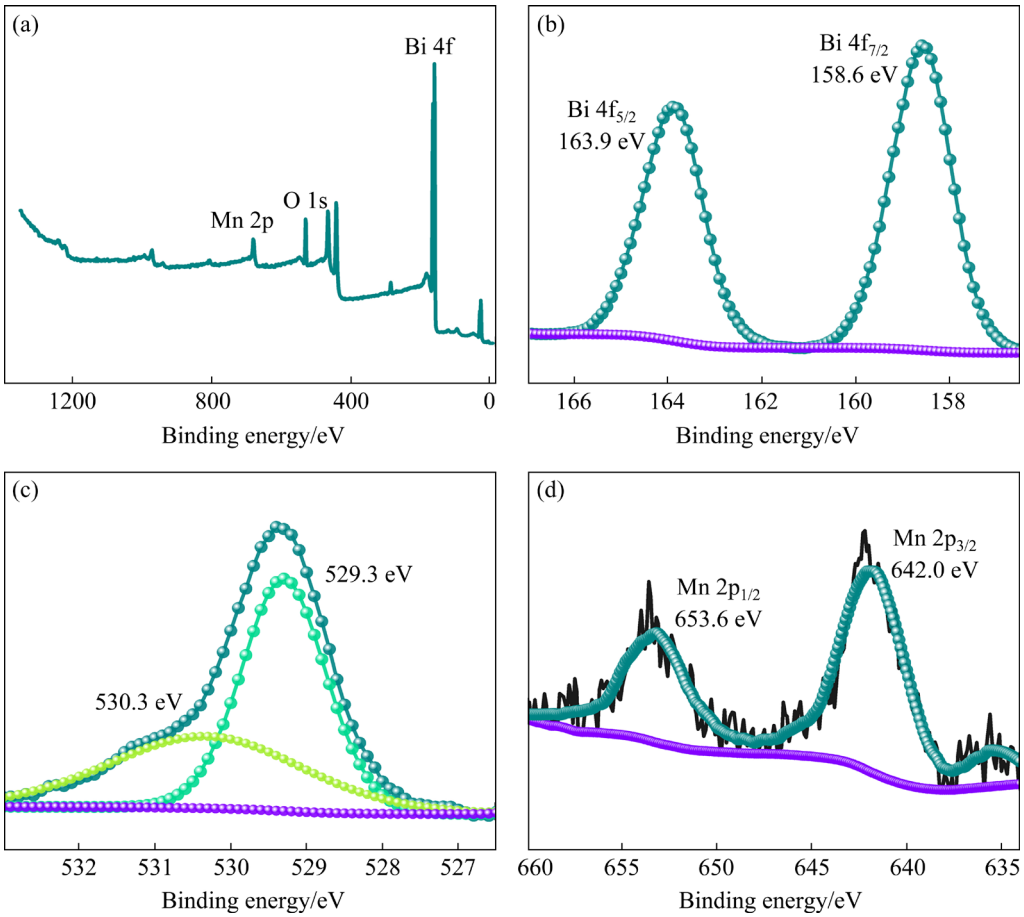

Fig. 3 Surface element and valence analysis: XPS survey (a), high-resolution spectra of Bi 4f (b), O 1s (c) and Mn 2p (d) for $Bi_{12}MnO_{20}$

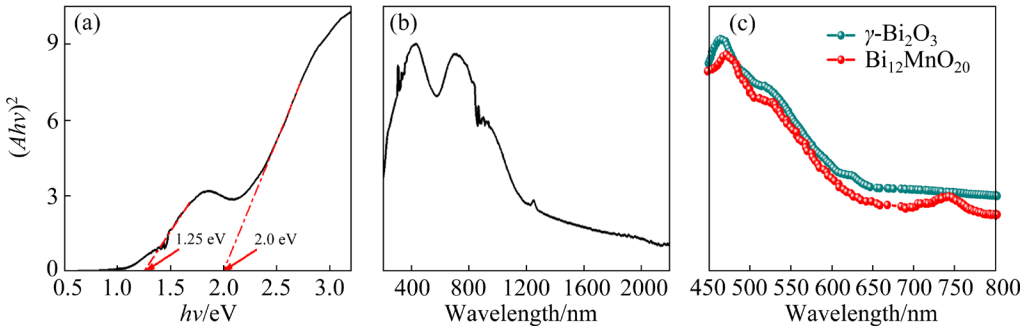

Fig. 4 Tauc plots for bandgap (a), UV–vis-Nir spectrum (b), and PL spectra (c) of $Bi_{12}MnO_{20}$

1.25 eV correspond to the inherent bandgap and sub-bandgap of $Bi_{12}MnO_{20}$, respectively. The intrinsic band gap of $Bi_{12}MnO_{20}$ is similar to those of other sillenite materials($Bi_{12}TiO_{20}$: 2.28 eV, $Bi_{12}CoO_{20}$:2.56 eV, $Bi_{12}FeO_{20}$: 2.1 eV), indicating that sillenite materials have high-energy light adsorption [13−15]. In addition, the existence of the sub-bandgap of $Bi_{12}MnO_{20}$ may be conducive to the separation of photo-generated charges in the photocatalytic process. As shown in Fig. 4(b), $Bi_{12}MnO_{20}$ can respond to the full solar-spectral of 200−2200 nm. The absorption peak at 400 nm in the UV range is derived from the intrinsic band gap of 2.0 eV. The absorption peak at 800 nm in the DRS curve implies the existence of the sub-bandgap of 1.25 eV in $Bi_{12}MnO_{20}$, which can facilitate the production of $^{\bullet}O_2^-$. Figure 4(c) demonstrates the PL spectra of the as-prepared $Bi_{12}MnO_{20}$ and γ-Bi_2O_3 with an excitation wavelength of 406.2 nm. It can be seen that the intense peak of $Bi_{12}MnO_{20}$ at 475 nm has a red-shift due to the hybridization of O 2p and Mn 3d orbital,

indicating the decrease of the photo-induced threshold for photocatalytic response compared with γ-Bi_2O_3 [25,26]. The weak emission peak of $Bi_{12}MnO_{20}$ at 740 nm attributes to the low recombination rate of photogenerated band edge free excitons and bound excitons on IB caused by the existence of a sub-band gap [26]. Meanwhile, the ionization of Bi—O—Mn framework caused by inhibiting the recombination of excitons can produce more active sites to produce $^{\bullet}O_2^-$ by absorbing O_2 in the solution [27]. What's more, $Bi_{12}MnO_{20}$ shows lower intensity than that of γ-Bi_2O_3 in the wavelength range of 450−800 nm, indicating the higher efficient separation rate of the carriers in $Bi_{12}MnO_{20}$.

3.3 Photocatalytic activity evaluation

The photocatalytic activity of $Bi_{12}MnO_{20}$ was evaluated by the variation of MG concentration (C/C_0) under full solar-spectrum light, and the results are shown in Fig. S4, Fig. 5 and 6. Figure S4 shows that the photocatalytic activity of $Bi_{12}MnO_{20}$ prepared at 500−700 °C decreases with the increase of calcination temperature. The reduction of photocatalytic activity is due to the decrease of active sites on the surface of photocatalysts prepared at high temperatures. From Fig. 5 and Table S1, the degradation rate significantly declines from 90.1% to 12.1% and the reaction rate constant reduces from 0.00724 to 0.00004 min^{-1} with the pH value of solution varying from the initial value (pH=4.86) to 3.0. In a low pH solution, the photogenerated electrons preferentially reduce H^+ ($\varphi(H^+/H_2)$=0 eV) rather than dissolved oxygen ($\varphi(O_2/^{\bullet}O_2^-)$=−0.33 eV), resulting in the absence of O_2^- as a kind of main active radical for oxidative decomposition.

Figure 6 represents the effect of different organic pollutants, initial concentration of pollutant and $Bi_{12}MnO_{20}$ concentration on photocatalytic degradation rate. As illustrated in Fig. 6(a), the photocatalytic degradation rates of MG, TC-HCl and RhB are 95.8%, 92.4% and 82.9%, respectively, indicating excellent photocatalytic activity of $Bi_{12}MnO_{20}$ to different organic pollutants at pH=8.0. As shown in Fig. S5, the TOC removal rate of simulated wastewater reaches 91.7% after 300 min with $Bi_{12}MnO_{20}$ under light irradiation, confirming

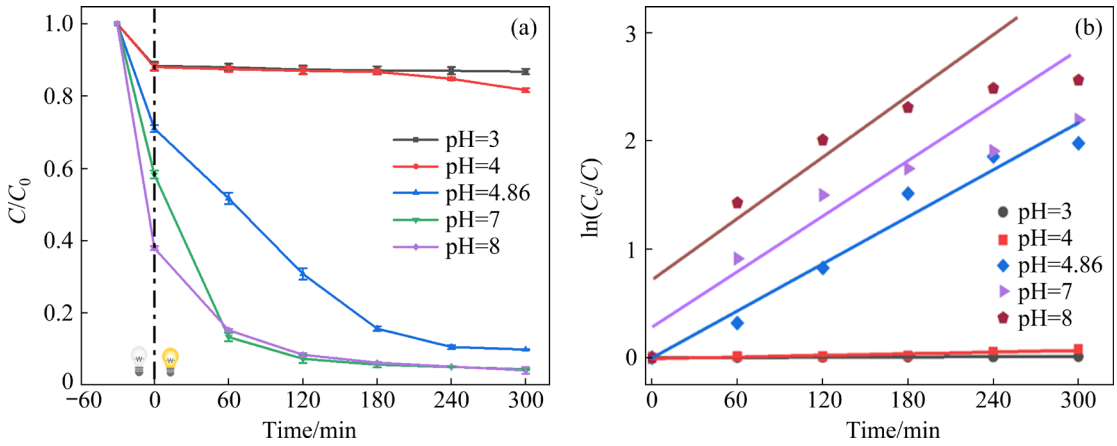

Fig. 5 Effect of pH on photocatalytic degradation (a) and reaction rate (b) of BMO to MG

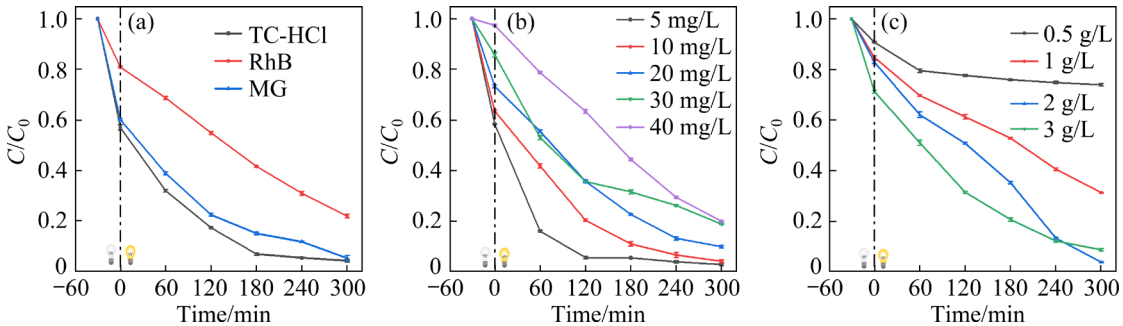

Fig. 6 Effect of different dyes (a), initial concentration of pollutant (b), and $Bi_{12}MnO_{20}$ concentration (c) on photocatalytic degradation rate

the mineralization of MG by $Bi_{12}MnO_{20}$ photocatalyst. The surface electronegativity of the organic pollutant in the alkaline solution is favorable to be adsorbed and oxidized by $\cdot O_2^-$ with high potential. In addition, the degradation rate of $Bi_{12}MnO_{20}$ for MG solution can remain above 80% for different concentrations of pollutants in 5 h (Fig. 6(b)). When the degradation time is 10 h, the degradation rate is up to 96.2% for the solution with 40 mg/L MG (Fig. S6), implying the possibility of degradation for the high-concentration organic pollutants. As illustrated in Fig. 6(c) and Table S2, the photocatalytic degradation rate of $Bi_{12}MnO_{20}$ increases substantially with the photocatalysis concentration from 0.5 to 2 g/L. When the concentration of $Bi_{12}MnO_{20}$ is over 3 g/L, the photodegradation efficiency has no significant increase. The excessive concentration of opaque $Bi_{12}MnO_{20}$ photocatalyst prevents solar light from entering the solution, resulting in a decrease in photogenerated electrons.

Figure 7 shows the photocatalytic degradation of MG by $Bi_{12}MnO_{20}$ photocatalyst under various light irradiation. As shown in Fig. 7, MG cannot be removed effectively under light irradiation without the addition of $Bi_{12}MnO_{20}$. In the presence of $Bi_{12}MnO_{20}$ photocatalyst, the degradation rates of MG in solution with and without light irradiation were 95.8% and 30.4%, respectively, implying photocatalytic degradation rather than physical adsorption. Moreover, $Bi_{12}MnO_{20}$ shows good photocatalytic activity for MG degradation under ultraviolet and visible light irradiation. In particular, the degradation rate of MG in solution by $Bi_{12}MnO_{20}$ was more than 60% under the irradiation of NIR light, indicating that $Bi_{12}MnO_{20}$ has excellent photo-response in the range of NIR light (see Fig. 4(b)).

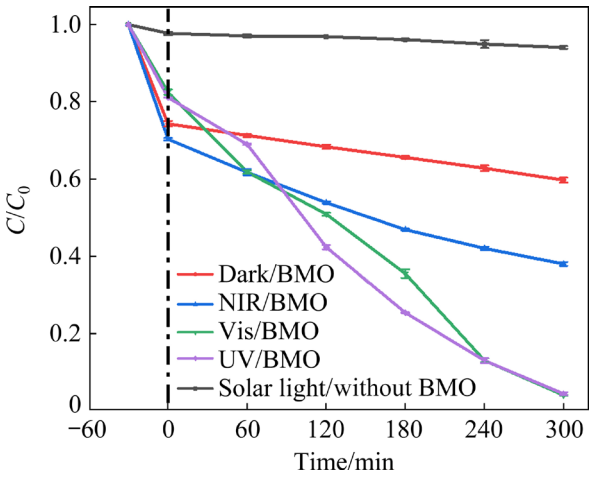

Fig. 7 Photocatalytic degradation of MG solution by various lights irradiation

To further investigate the stability and recyclability of $Bi_{12}MnO_{20}$ photocatalyst, four cycles of photocatalysis degradation tests were conducted and the results are displayed in Fig. 8. As shown in Fig. 8(a), the degradation rate of $Bi_{12}MnO_{20}$ for MG remains 74.9% after four cycles of photocatalysis reaction, indicating high reusability of $Bi_{12}MnO_{20}$. In addition, there are no obvious composition and structure changes from the XRD patterns (Fig. 8(b)) and FTIR (Fig. S7) of $Bi_{12}MnO_{20}$ after the recycling experiments, demonstrating nice stability of the photocatalyst.

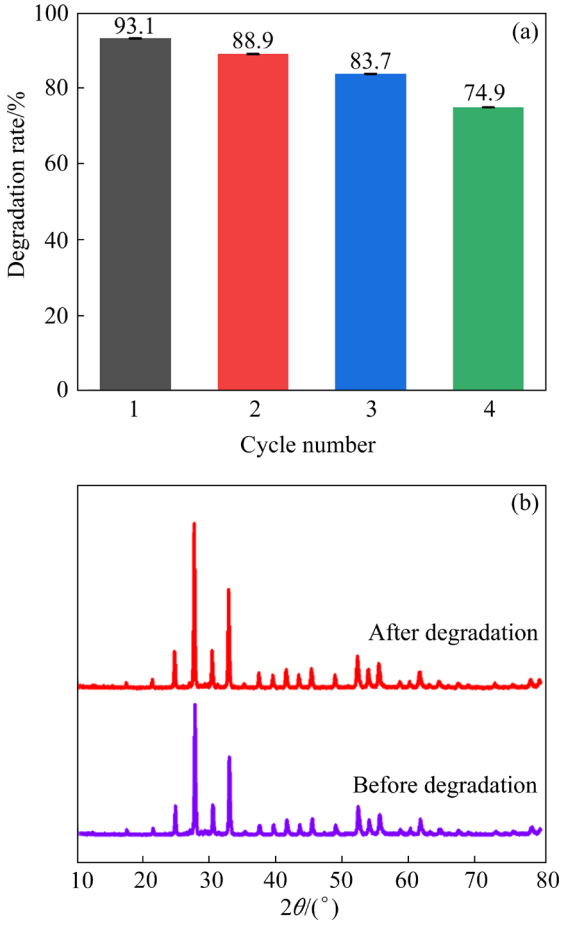

Fig. 8 Reusability and stability analysis of $Bi_{12}MnO_{20}$: (a) Cycling degradation; (b) XRD patterns before and after degradation

3.4 Photocatalytic mechanism

To confirm the main active radicals in the degradation of the MG solution by $Bi_{12}MnO_{20}$ photocatalysis, scavenger trapping experiments and

ESR tests were carried out. As shown in Fig. 9(a), the addition of BQ can significantly reduce the photocatalytic activity of $Bi_{12}MnO_{20}$, followed by AO, and the role of IPA is almost negligible, indicating that $^{\cdot}O_2^-$ is the primary active radical in this degradation process followed by h^+, and nearly no $^{\cdot}OH$ participates in the reaction. Figure 9(b) illustrates the reaction kinetic of $Bi_{12}MnO_{20}$ in different scavenger systems. The calculated k values for the BQ (0.0016 min^{-1}) system and AO (0.0046 min^{-1}) are smaller than that of the IPA (0.0082 min^{-1}) system with and no additives (0.0083 min^{-1}) system, demonstrating the crucial role of $^{\cdot}O_2^-$ in the photocatalytic process (Table S3). Furthermore, the ESR trapping experiment was explored to further verify the above-mentioned active radicals generated in the light-responsive photocatalytic process. As shown in Fig. 9(c), no signal of DMPO-$^{\cdot}O_2^-$ is detected under the dark, while obvious signal peaks of sample $Bi_{12}MnO_{20}$ are found under irradiation, demonstrating the production of $^{\cdot}O_2^-$ in the system under simulated sunlight. Moreover, $Bi_{12}MnO_{20}$ possesses a superior ability for the formation of $^{\cdot}O_2^-$ compared with γ-Bi_2O_3 due to the Mn doping [20,22]. There is no characteristic signal of DMPO-•OH in both dark and light conditions (Fig. 9(d)), indicating no •OH produced in the photocatalytic process.

The XPS valence band spectrum was used to obtain the band structure of $Bi_{12}MnO_{20}$. As shown in Fig. 10(a), the XPS potential of the VBM of $Bi_{12}MnO_{20}$ is 1.20 eV which can be converted to 1.31 eV (vs normal hydrogen electrode) according to the formula of $E_{NHE}=\phi+E_{VB-XPS}-4.44$, where E_{VB-XPS} is 1.20 eV obtained from the VB-XPS spectra, ϕ is 4.55 as the work function of the XPS analyzer, and E_{NHE} is the normal hydrogen electrode potential. The CBM value of $Bi_{12}MnO_{20}$ is calculated as −0.69 eV according to the formula $E_g=E_{VBM}-E_{CBM}$. The position of the intermediate band bottom (IBM) was deduced to 0.56 eV referring to sub-bandgap value (1.25 eV) and the CBM potential (1.31 eV).

Figure 10(b) shows Mott-Schottky (MS) plots of $Bi_{12}MnO_{20}$ and γ-Bi_2O_3. According to the MS equation, the plot has the potential as the horizontal

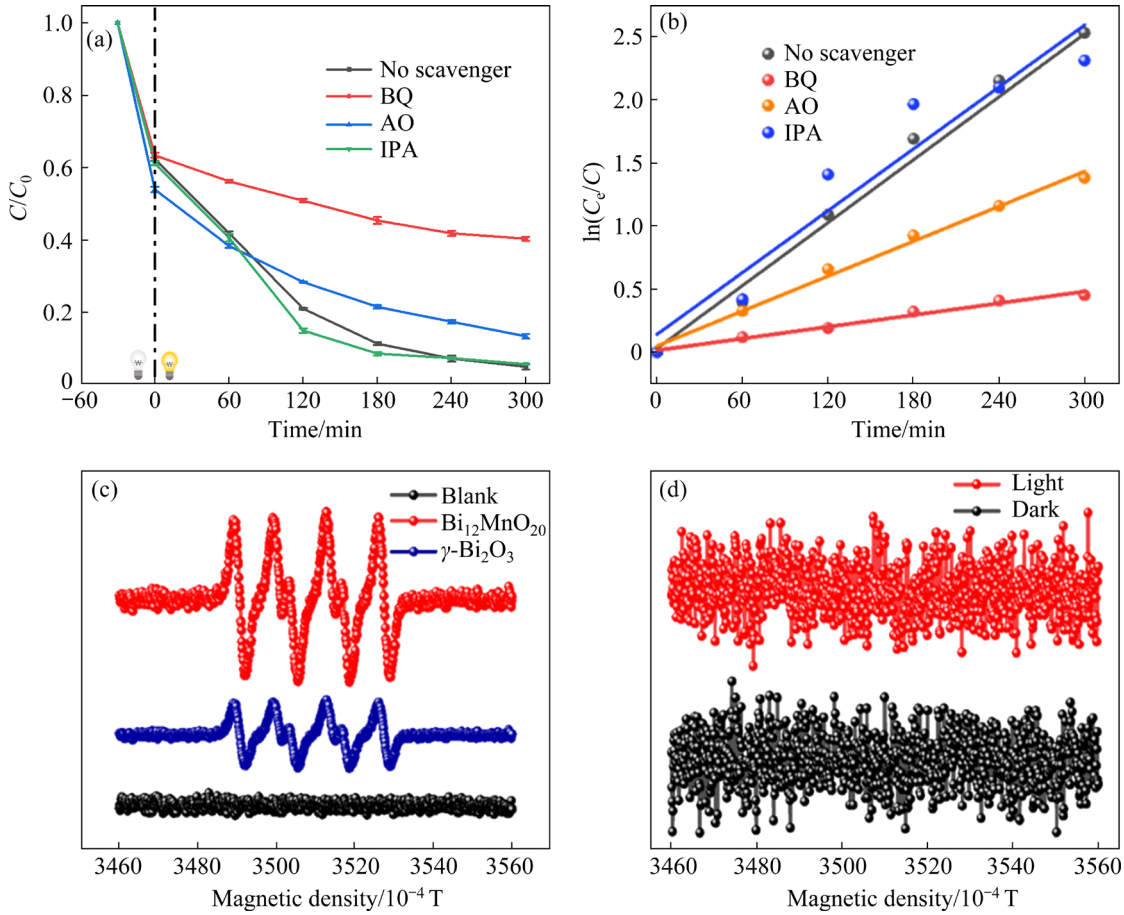

Fig. 9 Exploration and analysis of free radical types: Active species trapping experiments over $Bi_{12}MnO_{20}$ (a, b), and ESR spectra of DMPO-$^{\cdot}O_2^-$ (c), and DMPO-$^{\cdot}OH$ (d) for $Bi_{12}MnO_{20}$

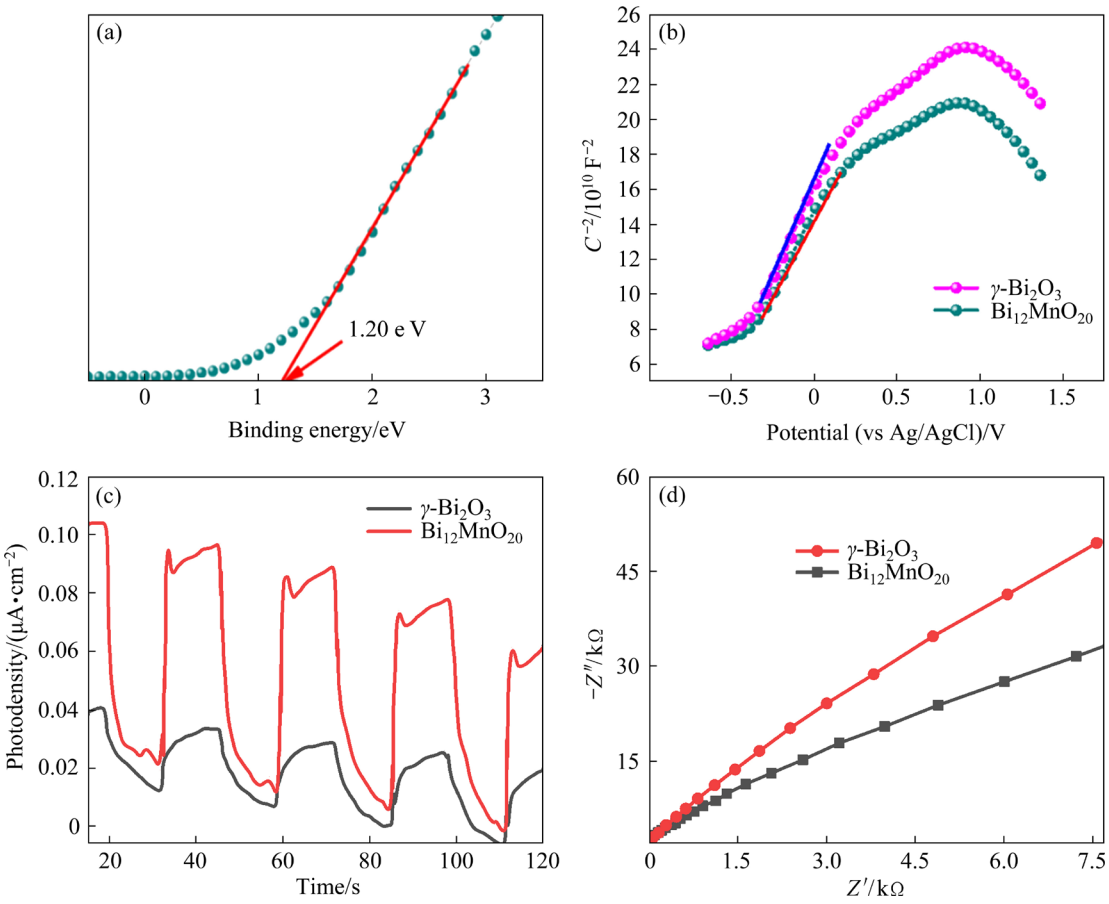

Fig. 10 XPS valence band spectrum of $Bi_{12}MnO_{20}$ (a), MS plots (b), photocurrent (c) and EIS (d) of $Bi_{12}MnO_{20}$ and γ-Bi_2O_3

coordinate and inverse square of the interface capacitance (C^{-2}) as the longtitudinal coordinate. As displayed in Fig. 10(b), both MS curves exhibit a positive slope, suggesting that $Bi_{12}MnO_{20}$ and γ-Bi_2O_3 are the n-type semiconductors. Additionally, the hill has the capability of investigating sample charge density. The slope of the curve for $Bi_{12}MnO_{20}$ is smaller than that for γ-Bi_2O_3, implying the increase of charge density in $Bi_{12}MnO_{20}$ due to the incorporation of Mn^{4+} ion, improving charge transfer of $Bi_{12}MnO_{20}$ [27,28]. Moreover, the separation efficiency for the photoinduced carriers of the photocatalysts was assessed by photocurrent analysis and EIS, as shown in Figs. 10(c) and (d). The photogenerated current of $Bi_{12}MnO_{20}$ is higher than that of γ-Bi_2O_3 (Fig. 10(c)), suggesting $Bi_{12}MnO_{20}$ with more effective separation of the photogenerated carriers during the photocatalytic reaction. Further, the radius of Nyquist circle for $Bi_{12}MnO_{20}$ is smaller than that of pure γ-Bi_2O_3 (Fig. 10(d)), indicating the charge-transfer efficiency of $Bi_{12}MnO_{20}$.

Based on the above results, the photocatalytic mechanism of $Bi_{12}MnO_{20}$ was proposed and displayed in Fig. 11. As depicted in Fig. 11(a), the CBM potential (−0.69 eV) of $Bi_{12}MnO_{20}$ is more negative than the redox potential of $O_2/{}^{\bullet}O_2^-$ (−0.33 eV), thus photogenerated e can reduce dissolved O_2 in solution to produce ${}^{\bullet}O_2^-$. Meanwhile, the sub-bandgap provides an intermediate transition level for e to CBM, which promotes the generation of ${}^{\bullet}O_2^-$. The VBM potential (1.31 eV) of $Bi_{12}MnO_{20}$ is less positive than the redox potential of $OH^-/{}^{\bullet}OH$ (1.90 eV) and $H_2O/{}^{\bullet}OH$ (2.27 eV), indicating that it is difficult for h^+ to oxidize H_2O or OH^- into ${}^{\bullet}OH$ [29−31]. The photo-oxidation process of $Bi_{12}MnO_{20}$ driven by full spectral light can be established as shown in Fig. 11(b). When solar light irradiates the $Bi_{12}MnO_{20}$, the electrons in IBM and VBM of $Bi_{12}MnO_{20}$ can be excited to CBM, leaving h^+ in IBM and VBM. Photogenerated h^+ can attack MG directly without the formation of •OH [32]. The e in CBM can react with the oxygen dissolved in solution to produce ${}^{\bullet}O_2^-$, which can degrade the

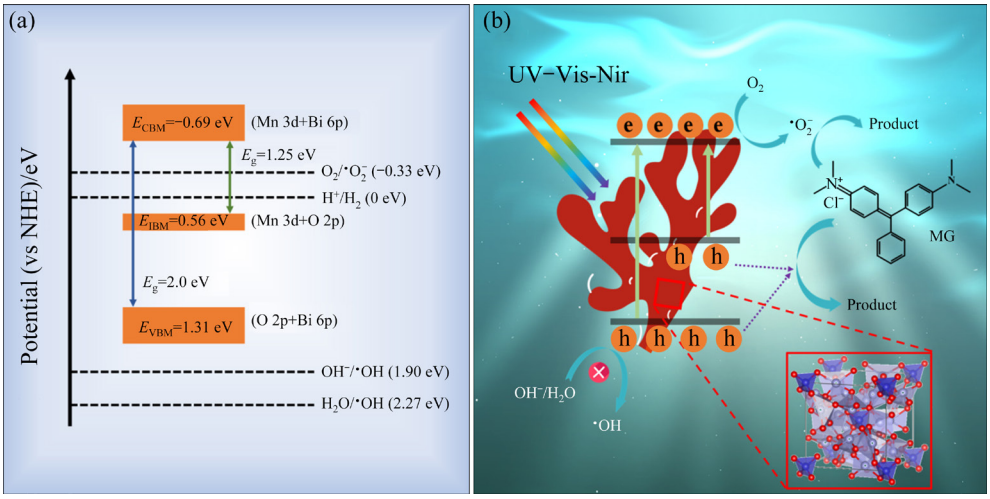

Fig. 11 Band structure (a) and photocatalytic mechanism (b) of $Bi_{12}MnO_{20}$

organic molecules [33]. Meanwhile, the sub-bandgap formed by Mn^{4+} doping in $Bi_{12}MnO_{20}$ provides the intermediate level for e transfer from IB to CB, enhancing the generation of $^{\bullet}O_2^-$, and improving the separation of carrier pairs [34]. This high carrier utilization efficiency endows $Bi_{12}MnO_{20}$ with excellent photodegradation activity to MG. The photodegradation reaction equations are listed as follows:

$$Bi_{12}MnO_{20}+h\nu \rightarrow h^+ (VBM)+h^+ (IBM)+e (CBM) \quad (1)$$

$$e (CBM)+O_2 \rightarrow {}^{\bullet}O_2^- \quad (2)$$

$$MG+{}^{\bullet}O_2^- \rightarrow CO_2+products \quad (3)$$

$$MG+h^+ (VBM) \rightarrow products \quad (4)$$

$$MG+h^+ (IBM) \rightarrow products \quad (5)$$

4 Conclusions

(1) Coral-like sillenite-type $Bi_{12}MnO_{20}$ photocatalyst with the pore volume of 0.02 cm^3/g and the specific surface area of 3.585 m^2/g was prepared by wet ball milling followed by calcination. The formation of sub-bandgap by the incorporation of Mn^{4+} into cubic γ-Bi_2O_3 lattice is beneficial to improving the Vis-NIR light response capability.

(2) The existence of the sub-bandgap in $Bi_{12}MnO_{20}$ improves the generation of $^{\bullet}O_2^-$ and the separation of carrier pairs.

(3) The degradation efficiency of MG by $Bi_{12}MnO_{20}$ reaches 95.8% with 5 h under simulated sunlight. After four cycles of photocatalysis degradation, the removal rate of MG by $Bi_{12}MnO_{20}$ remains at 74.9%, indicating the high stability and reusability of $Bi_{12}MnO_{20}$. This work sheds light on the underpinnings of the photocatalytic properties of $Bi_{12}MnO_{20}$ with potential application in contaminants purification.

Acknowledgments

This work was financially supported by the National Natural Science Foundation of China (No. 51974378), the Natural Science Foundation of Hunan province, China (No. 2020JJ4735), and the Hunan Key Laboratory for Rare Earth Functional Materials, China (No. 2017TP1031).

Supplementary Information

Supplementary Information in this paper can be found at: http://tnmsc.csu.edu.cn/download/26-p3570-2022-1255-Supplementary_Information.pdf.

References

[1] LIN Angela Yu-chen, WANG Xiao-huan, LEE Wan-ning. Impact of wastewaters and hospital effluents on the occurrence of controlled substances in surface waters [J]. Chemosphere, 2010, 81(5): 562−570.

[2] WANG Zheng-lu, XU Ze-qiong, Li Xi-qing. Biodegradation of methamphetamine and ketamine in aquatic ecosystem and associated shift in bacterial community [J]. Journal of Hazardous Materials, 2018, 359: 356−364.

[3] BAKER D R, KASPRZYK-HORDERN B. Spatial and temporal occurrence of pharmaceuticals and illicit drugs in the aqueous environment and during wastewater treatment: new developments [J]. Science of the Total Environment, 2013, 454/455: 442−456.

[4] YANG Gao-chen, PAN Qi-yun, YANG Peng, LIU Yi-si, DU Yue, WANG Kai. Heteropolyacids supported on

hierarchically macrolmesoporoscs TiO_2: Efficient catalyst for deep oxidative desulfurization of fuel [J]. Tungsten, 2022, 4(1): 28−37.

[5] WANG Song-can, YUN Jung-ho, LUO Bin, BUTBUREE T, PEERAKIATKHAJOHN P, THAWEESAK S, XIAO Mu, WANG Lian-zhou. Recent progress on visible light responsive heterojunctions for photocatalytic applications [J]. Journal of Materials Science & Technology, 2017, 33(1): 1−22.

[6] ZHANG Hai-tao, FENG Yuan-ting, JIA Shi-cheng, JIANG Dong-mei, ZHAN Qing-feng. Enhancing the photocatalytic performance of $Bi_{12}SiO_{20}$ by in situ grown $Bi_2O_2CO_3$ and Bi through two-step light irradiation method [J]. Applied Surface Science, 2020, 520: 146355.

[7] LIU Hong-xia, MEI Hui, MIAO Nan-xi, PAN Long-kai, JIN Zhi-peng, ZHU Gang-qiang, GAO Jian-zhi, WANG Jun-jie, CHENG Lai-fei. Synergistic photocatalytic NO removal of oxygen vacancies and metallic bismuth on $Bi_{12}TiO_{20}$ nanofibers under visible light irradiation [J]. Chemical Engineering Journal, 2021, 414: 128748.

[8] CHANG Fei, ZHANG Xiao-ya, YANG Cheng, PENG Shi-jie, HU Xue-feng. Ag nanoparticles-embellished $Bi_{12}GeO_{20}$ composites: A plasmonic system featured with reinforced visible-light photocatalytic performance and ultra-stability [J]. Applied Surface Science, 2020, 527: 146946.

[9] LI Kai, HUANG Zhen-yu, ZENG Xiao-qiao, HUANG Bai-biao, GAO Shan-min, LU Jun. Synergetic effect of Ti^{3+} and oxygen doping on enhancing photoelectrochemical and photocatalytic properties of TiO_2/g-C_3N_4 heterojunctions [J]. ACS Applied Materials & Interfaces, 2017, 9(13): 11577−11586.

[10] CUI Zhan-kui, SONG Hong-tao, GE Su-xiang, HE Wei-wei, LIU Yu-wen. Fabrication of BiOCl/BiOBr hybrid nanosheets with enhanced superoxide radical dominating visible light driven photocatalytic activity [J]. Applied Surface Science, 2019, 467/468: 505−513.

[11] DENG Q R, XIA X H, GUO M L, GAO Y, SHAO G. Mn-doped TiO_2 nanopowders with remarkable visible light photocatalytic activity [J]. Materials Letters, 2011, 65(13): 2051−2054.

[12] JIANG Li-sha, WANG Kai, WU Xiao-yong, ZHANG Gao-ke, YIN Shu. Amorphous bimetallic cobalt nickel sulfide cocatalysts for significantly boosting photocatalytic hydrogen evolution performance of graphitic carbon nitride: Efficient interfacial charge transfer [J]. ACS Applied Materials & Interfaces, 2019, 11(30): 26898−26908.

[13] BAALOUDJ O, NASRALLAH N, BOUALLOUCHE R, KENFOUD H, KHEZAMI L,ASSADI A A. High efficient Cefixime removal from water by the sillenite $Bi_{12}TiO_{20}$: Photocatalytic mechanism and degradation pathway [J]. Journal of Cleaner Production, 2022, 330: 129934.

[14] KENFOUD H, BAALOUDJ O, NASRALLAH N, BAGTACHE R, ASSADI A A, TRARI M. Structural and electrochemical characterizations of $Bi_{12}CoO_{20}$ sillenite crystals: Degradation and reduction of organic and inorganic pollutants [J]. Journal of Materials Science-Materials in Electronics, 2021, 32: 16411−16420.

[15] VAVILAPALLI D S, MELVIN A A, BELLARMINE F, MANNAM R, VELAGA S, POSWAL H K, DIXIT A, RAMACHANDRA RAO M S, SINGH S. Growth of sillenite $Bi_{12}FeO_{20}$ single crystals: Structural, thermal, optical, photocatalytic features and first principle calculations [J]. Science Report, 2020, 10: 22052.

[16] CHEN Jun, ZHAN Jing, LI Qi-hou. Exploration and crystal phase engineering from bismuthinite ore to visible-light responsive photocatalyst of Bi_2O_3 [J]. Journal of Environmental Chemical Engineering, 2019, 7(5): 103375.

[17] WU Xiao-yong, LI Ming-meng, LI jun, ZHANG Gao-ke, YIN Shu. A sillenite-type $Bi_{12}MnO_{20}$ photocatalyst: UV, visible and infrared lights responsive photocatalytic properties induced by the hybridization of Mn 3d and O 2p orbitals [J]. Applied Catalysis B: Environmental, 2017, 219: 132−141.

[18] BAALOUDJ O, KENFOUD H,BADAWI A K, ASSADI A A, EL JERY A, ASSADI A A, AMRANE A. Bismuth sillenite crystals as recent photocatalysts for water treatment and energy generation: A critical review [J]. Catalysts, 2022, 12(5): 500.

[19] YANG Gui-hua, MIAO Wen-kang, YUAN Zhi-min, JIANG Zai-yong, HUANG Bai-biao, WANG Peng, CHEN Jia-chuan. Bi quantum dots obtained via in situ photodeposition method as a new photocatalytic CO_2 reduction cocatalyst instead of noble metals: Borrowing redox conversion between Bi_2O_3 and Bi [J]. Applied Catalysis B: Environmental, 2018, 237: 302−308.

[20] WAN Zhen, ZHANG Gao-ke, WU xiao-yong, YIN Shu. Novel visible-light-driven Z-scheme $Bi_{12}GeO_{20}$/g-C_3N_4 photocatalyst: Oxygen-induced pathway of organic pollutants degradation and proton assisted electron transfer mechanism of Cr(VI) reduction [J]. Applied Catalysis B: Environmental, 2017, 207: 17−26.

[21] JIN Lei, XU Lin-ping, MOREIN C, CHEN Chun-hu, LAI M, DHARMARATHNA S, DOBLEY A, SUIB S L. Titanium containing γ-MnO_2 (TM) hollow spheres: One-step synthesis and catalytic activities in Li/air batteries and oxidative chemical reactions [J]. Advanced Functional Materials, 2010, 20(19): 3373−3382.

[22] KOSTOWSKYJ M A, KIRK D W, THORPE S J. Ag and Ag−Mn nanowire catalysts for alkaline fuel cells [J]. International Journal of Hydrogen Energy, 2010, 35(11): 5666−5672.

[23] GENG Yan-xian, CHEN Dong-yun, LI Na-jun, XU Qing-feng, LI Hua, HE Jing-hui, LU Jian-mei. Z-Scheme 2D/2D α-Fe_2O_3/g-C_3N_4 heterojunction for photocatalytic oxidation of nitric oxide [J]. Applied Catalysis B: Environmental, 2021, 280: 119409.

[24] ZHAO Zong-yan. Application of theoretical calculation and simulation in photocatalysis [M]. Beijing: Research Science Press, 2014.

[25] WANG Chu-ya, ZHANG Xing, QIU Hai-bin, HUANG Gui-xiang, YU Han-qing. $Bi_{24}O_{31}Br_{10}$ nanosheets with controllable thickness for visible-light-driven catalytic degradation of tetracycline hydrochloride [J]. Applied Catalysis B: Environmental, 2017, 205: 615−623.

[26] QIAO Xue-bin, PU Yin-fu, LI Yu-ze, HUANG Yan-lin, CHENG Han, SEO H J. Structural characteristics and photocatalytic ability of vanadate-sillenite $Bi_{25}VO_{40}$

nanoparticles [J]. Powder Technology, 2016, 287: 277−284.
[27] SAKTHIVEL S, NEPPOLIAN B, SHANKAR M V, ARABINDOO B, PALANICHAMY M, MURUGESAN V. Solar photocatalytic degradation of azo dye: Comparison of photocatalytic efficiency of ZnO and TiO_2 [J]. Solar Energy Materials and Solar Cells, 2003, 77(1): 65−82.
[28] ZENG Jian, XU Liang, LUO Xin, CHEN Tong, TANG Shuai-hao, HUANG Xin, WANG Ling-ling. *Z*-scheme systems of ASi2N4 (A=Mo or W) for photocotalytic water splitting and nonogenerators [J]. Tungsten, 2022, 4(1): 52−59.
[29] HUANG Hao-wei, ZHOU Chen, JIAO Xing-chen, YUAN Hai-feng, ZHAO Ji-wu, HE Chun-qing, HOFKENS J, ROEFFAERS M B J, LONG Jin-lin, STEELE J A. Subsurface defect engineering in single-unit-cell Bi_2WO_6 monolayers boosts solar-driven photocatalytic performance [J]. ACS Catalysis, 2020, 10(2): 1439−1443.
[30] DVORANOVÁ D, BARBIERIKOVÁ Z, BREZOVÁ V. Radical intermediates in photoinduced reactions on TiO_2 [J]. Molecules, 2014, 19(11): 17279−17304.
[31] HAUNG Hao-wei, YUAN Hai-feng, JANSSEN K P F, SOLÍS-FERNÁNDEZ G, WANG Ying, TAN C Y X, JONCKHEERE D, DEBROYE E, LONG Jin-lin, HENDRIX J, HOFKENS J, STEELE J A, ROEFFAERS M B J. Efficient and selective photocatalytic oxidation of benzylic alcohols with hybrid organic-inorganic perovskite materials [J]. ACS Energy Letters, 2018, 3(4): 755−759.
[32] LI Wen-xuan, WANG Zhuang-zhuang, LI Yuan, GHASEMIAND J, LI Jun, ZHANG Gao-ke. Visible-NIR-light responsive 0D/2D CQDs/Sb_2WO_6 nanosheets with enhanced photocatalytic degradation performance of RhB: Unveiling the dual roles of CQDs and mechanism study [J]. Journal of Hazardous Materials, 2022, 424: 127595.
[33] REN Yu-yu, LI Yuan, WU Xiao-yong, WANG Jin-long, ZHANG Gao-ke. S-scheme Sb_2WO_6/g-C_3N_4 photocatalysts with enhanced visible-light-induced photocatalytic NO oxidation performance [J]. Chinese Journal of Catalysis, 2021, 42(1): 69−77.
[34] BAKHTIARNIA S, SHEIBANI S, BILLARD A, AUBRY E, ARAB POUR YAZDI M. Deposition of nanoporous $BiVO_4$ thin-film photocatalyst by reactive magnetron sputtering: Effect of total pressure and substrate [J]. Transactions of Nonferrous Metals Society of China, 2022, 32(3): 957−971.

软铋矿 $Bi_{12}MnO_{20}$ 的制备及利用超氧自由基提升其去除有机污染物光催化活性

湛 菁[1]，王焕伟[1]，李启厚[1]，王志坚[2]，房 鑫[1]

1. 中南大学 冶金与环境学院，长沙 410083；
2. 湖南稀土金属材料研究院，长沙 410083

摘 要：通过湿法球磨联合煅烧方法制备软铋矿型光催化材料 $Bi_{12}MnO_{20}$，其光吸收能力覆盖 200～2200 nm 光谱范围。$Bi_{12}MnO_{20}$ 的晶体结构可以视为 Mn^{4+} 掺入到亚稳立方 γ-Bi_2O_3 的四面体中所得，并且 $Bi_{12}MnO_{20}$ 的能带结构中出现禁带宽度为 1.25 eV 的子带隙。这种能带结构的优化有利于 $Bi_{12}MnO_{20}$ 光催化剂加速转化溶液中 O_2 为超氧自由基($\cdot O_2^-$)，以改善光催化降解过程中的电荷分离和转移。结果表明，在模拟阳光照射下，$Bi_{12}MnO_{20}$ 对 pH 8 溶液中浓度为 10 mg/L 的孔雀石绿降解率达到 95%以上。经过 4 次光降解实验后，$Bi_{12}MnO_{20}$ 对孔雀石绿的降解率保持在 74.9%。

关键词：$Bi_{12}MnO_{20}$；光催化；降解；能带；超氧自由基

(Edited by Xiang-qun LI)